High Resolution Intravascular MRI and MRS by Using a Catheter Receiver Coil

Ergin Atalar, Paul A. Bottomley, Ogan Ocali, Luis C. L. Correia, Mark D. Kelemen, Joao A. C. Lima, Elias A. Zerhouni

Potentially important diagnostic information about atherosclerosis can be obtained by using magnetic resonance imaging and spectroscopy techniques. Because critical vessels such as the aorta, coronary arteries, and renal arteries are not near the surface of the body, surface coils are not adequate to increase the data quality to desired levels. A few catheter MR receiver coil designs have been proposed for imaging the walls of large blood vessels such as the aorta. These coils have limited longitudinal coverage and they are too thick to be placed into small vessels. A flexible, long and narrow receiver coil that can be placed on the tip of a catheter and will enable multi-slice high resolution imaging of small vessels has been developed. The authors describe the theory of the coil design technique, derive formulae for the signal-to-noise ratio characteristics of the coil, and show examples of high resolution cross-sectional images from isolated human aortas acquired by using this catheter coil. In addition, high resolution *in vivo* rabbit aorta images were obtained as well as a set of spatially resolved chemical shift spectra from a dog circumflex coronary artery.

Key words: intravascular MRI; MR catheter coil; atherosclerosis; MRI of arterial wall.

INTRODUCTION

Atherosclerotic disease is a major cause of mortality and morbidity. Localized forms of the disease, such as plaques, can compromise regional blood flow and require intervention in many cases. Although angiography is effective in detecting luminal narrowing, it reveals very little about the lesions themselves. Therapeutic methods such as intravascular intervention suffer from relatively high failure rates partly because of the lack of valid animal models and no detailed information on the pathologic plaques (1). An imaging method capable of providing detailed qualitative and quantitative data on the status of vascular walls at the time of intervention could favorably influence patient outcomes by enabling clinicians to select the best intervention method and provide precise guidance for various forms of local therapy. This problem has attracted considerable interest and has led to the development of angioscopy (2) and intravascular ultrasound (3), which are currently the only clinically approved methods for visualizing plaques. Angioscopy provides limited information about the surface of the vessel wall. Intravascular ultrasound also suffers from several drawbacks: its insensitivity to soft tissue and the inability to reliably detect thrombus (new or organized) superimposed on soft, lipid-laden plaques (3); artifacts related to transducer angle relative to the wall; an imaging plane limited to the aperture of the transducer; and variable resolution at different depths of view.

The use of MR scanners as x-ray-less fluoroscopes for minimally invasive procedures offers great potential for the performance of therapeutic intravascular procedures. Recently, several open-architecture magnets that permit direct access to the patient by an operator have been introduced in the marketplace for such purposes. More research needs to be done, but the implementation of new therapeutic and diagnostic approaches employing MR will be significantly enhanced by the development of novel intravascular high resolution MR imaging techniques. These techniques would provide morphologic information about atherosclerotic plaques, and MR spectroscopy methods would provide information about their chemical composition.

It has been shown *in vitro* that MR microimaging can identify and quantify atherosclerotic lesions (4–7). Recent technological advances in MRI techniques allow very high resolution images with short data acquisition times. Yuan *et al.* (8) used a fast spin echo MR imaging technique to image atherosclerotic plaques on an isolated vessel that had been removed at the time of carotid endarterectomy. Since signal-to-noise ratio (SNR) decreases with decreasing voxel size, special RF receiver coils were designed. These authors showed that at 1.5 T, it is possible to discriminate foam cells, fibrous plaque, organized thrombi, new thrombi, areas of loose necrosis, and calcium using various T_1- and T_2-weighted pulse sequences. Recently, Martin *et al.* (9) performed high resolution imaging of human arteries by using dedicated surface coils. They demonstrated that MR imaging findings correlated reliably with tissue type. Lipid deposits in isolated human atheroma have also been imaged by using special coils (10, 11). Other investigators showed that the fat content of atherosclerotic plaques can be determined by using chemical shift imaging (12–14). These studies indicate that MR has the potential for fully characterizing vessel wall disease but suffers from low anatomic resolution unless used *in vitro* on small specimens with high resolution methods.

Furthermore, with the recent development of better gradient systems, with up to 200–250 T/s/m slew rates on clinical scanners, real-time imaging is now routinely possible. With echo-planar imaging (EPI) systems, 10 images/s are achievable and allow guidance and local-

MRM 36:596–605 (1996)

From the Johns Hopkins University School of Medicine, Department of Radiology and Division of Cardiology (L.C.L.C., M.D.K., J.A.C.L.), Baltimore, Maryland.

Address correspondence to: Ergin Atalar, Ph.D., Department of Radiology, Johns Hopkins University School of Medicine, 601 N. Caroline St. JHOC 4241, Baltimore MD 21287-0845.

Received October 26, 1995; revised April 24, 1996; accepted April 25, 1996.

This work was supported by the Whitaker Foundation.

0740-3194/96 $3.00

ization of intravascular devices, as demonstrated by Dumoulin *et al.* (15). Koechli *et al.* (16) recently discussed the MR compatibility characteristics of various catheter and guide wire systems for use in interventional MR procedures.

High resolution imaging of atherosclerotic plaques is optimally achieved by a coil placed closed to the target vessel. A catheter coil was designed by Kantor *et al.* (17) to improve the SNR of ^{31}P spectroscopy of the canine heart. They examined the right ventricle of beagles by inserting the catheter coil through the jugular vein. Later, two independent groups (18, 19) developed catheter coils composed of opposed solenoidal coils to produce high resolution images of atherosclerotic plaques. Recently, Martin and Henkelman (20) demonstrated high resolution imaging of a live animal using this system. Single-loop multi-turn RF coils were designed and tested on human arterial specimens by Kandarpa *et al.* (21). The disadvantages of these designs are that the coils are rigid and too large to place into small diseased vessels. Unfortunately, most of the vessels of interest (such as coronary arteries) tend to be tortuous, and a catheter placed in these vessels must be flexible and small. An additional disadvantage of these designs is that multi-slice acquisition is limited in longitudinal coverage to a few millimeters in the opposed solenoidal design and to 1–2 cm in the single loop, multi-turn design.

We have developed a new flexible, long and narrow catheter RF receiver coil of a novel geometry that enables high resolution multi-slice MR imaging and high resolution one-dimensional (1D) chemical shift imaging (1D CSI) of small tortuous vessels in any orientation relative to the main magnetic field. This catheter coil is composed of two parallel conductors with a shorted end (Fig. 1). In this paper, we describe the theory of the coil design technique, and derive formulae for the SNR characteristics of the coil. We show examples of high resolution cross-sectional images from isolated human aortas acquired by using this catheter coil and demonstrate a set of spatially resolved chemical shift spectra from a dog circumflex coronary artery.

THEORY

We designed a coil composed of two parallel conductors. The conductors are shorted at one end, and the other end is used as the terminal of the coil (see Fig. 1). A plastic (vinyl) insulator covers the conductors. The coil works in blood or in saline solution. The maximum diameter of the catheter receiver coil is determined by the size of the vessel of interest. This elongated coil design enables multi-slice high resolution imaging and 1D CSI along the length of the coil, and the longitudinal coverage of the coils was the same as the length of the coils. Specific absorption rate in an intravascular MR experiment is the same as in a conventional MR experiment because the catheter coil is serving as a receiver coil and is off during RF transmission.

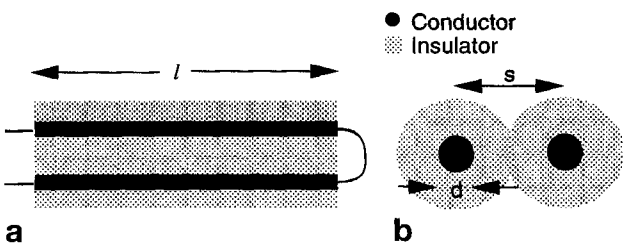

FIG. 1. Diagram of the catheter coil. (a) longitudinal view (b) axial view. The material between wires is dielectric and reduces the dielectric losses of the coil.

Electrical Model

By using transmission line theory, it is possible to formulate the electrical characteristics of the coil (22). Once one finds the circuit model of a differential length of transmission line (in our case, it is two parallel conductors), the electrical characteristics of any length of line can be calculated. The general electrical circuit model of a differential length of a generalized transmission line is shown in Fig. 2a. Let Z_s and Z_p be series and parallel impedances in the model. The impedance of the catheter coil is equal to the impedance of a transmission line with zero load (22):

$$Z = Z_0 \tanh(\gamma l) \qquad [1]$$

where $Z_0 = \sqrt{Z_p Z_s}$ is the characteristic impedance of the wire and is a function of the separation and the diameter of the conductors. ω is the larmor frequency in radians per second. j is the complex number $\sqrt{-1}$, l is the length of the cable and $\gamma = \sqrt{Z_s/Z_p}$ is the propagation constant.

For a catheter coil in a lossy medium such as blood, the electrical model is shown in Fig. 2b. In this model, L represents the inductance of the transmission line per unit length. R is the combination of conductor surface resistance and an equivalent resistance due to inductive losses. C_i and C_b are the capacitance resulting from charge stored in the insulator and in blood external to the coil, respectively, as shown in Fig. 3. G_i and G_b are equivalent conductances for the dielectric losses in a unit length of transmission line.

Standard formulae for inductance and capacitances are (from ref. 22):

$$L = \frac{\mu}{\pi} \cosh^{-1}(s/d) \qquad [2]$$

$$C_i \approx \frac{\pi \epsilon_0 \epsilon_i}{\ln(s/d)} \qquad [3]$$

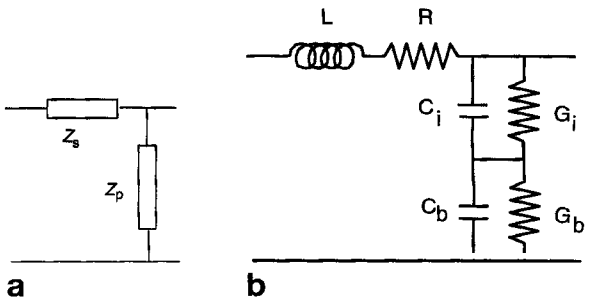

FIG. 2. The electrical model of transmission lines of differential length.

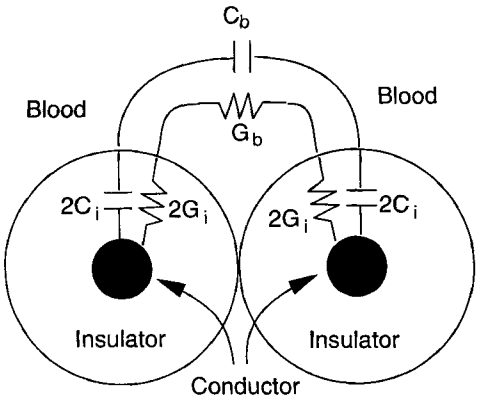

FIG. 3. The cross-sectional view of an insulated transmission line in blood.

$$C_b \approx \frac{\pi \epsilon_0 \epsilon_b}{\cosh^{-1}(s/d) - \ln(s/d)} \quad [4]$$

where s and d are the separation and diameter of the conductors. μ is the magnetic susceptibility and is almost the same in blood and insulator as in vacuum. ϵ_i and ϵ_b are the dielectric constants of the insulator and blood, respectively. ϵ_0 is the permittivity of the vacuum. For a 26AWG two-conductor cable with a conductor diameter (d) of 0.5 mm and a separation (s) of 1.6 mm, the inductance and capacitance values are calculated as shown in Table 1. In this calculation we assumed $\epsilon_b = 72.8$ (23)) and $\epsilon_i = 3.0$ (24). To verify these calculation results, we measured the open and short circuited impedances of pieces of the 26AWG cable with various lengths (116, 51, 24, and 10 cm) by using a vector impedance meter in the 64 ± 10 MHz range in both saline solution and air (saline and blood have very similar dielectric properties (23)). The series and parallel impedances (Z_s and Z_p values) of cable were estimated by using a numeric optimization (simulated annealing) algorithm (25). As expected, the series impedance was not significantly affected by the loading condition. The corresponding inductance values are listed as the measured values in Table 1. A change with a factor of 2.55 in the series impedance was observed depending on the loading condition. Since the capacitance is proportional to the dielectric constant, in the absence of blood, the capacitance resulting from interactions external to the coil will decrease to C_b/ϵ_b. Using this fact, we evaluated the measured C_b and C_i values as shown in Table 1. The theoretical results and measurements are in agreement, suggesting that the electrical model is correct.

Table 1
Comparison of Theoretical and Experimental Values of Inductance and Capacitances of the Electrical Circuit Model of a 26-AWG Dual Conductor Wire in Saline Solution

Parameter	Theory	Measurement
L_{loaded}	732 nH/m	750 nH/m
L_{unloaded}	732 nH/m	710 nH/m
C_i	72 pH/m	76 pF/m
C_b	3031 pF/m	3400 pF/m

Once C_i and C_b values are known, it is possible to calculate the conductance values by using the following formula:

$$G_i = \frac{\sigma_i C_i}{\epsilon_i \epsilon_0} \quad [5]$$

$$G_b = \frac{\sigma_b C_b}{\epsilon_b \epsilon_0} \quad [6]$$

where σ_i and σ_b are the conductivity of the insulator and blood at the larmor frequency, respectively. For the 26AWG wire, G_i and G_b values can be calculated as 7×10^{-11} and 6.8 υ/m. For this calculation, σ_b and σ_i were taken as 1.3 υ/m (23) and 2.5×10^{-11} υ/m (24), respectively.

Neglecting inductive losses from induced eddy currents in the surrounding medium, the surface resistance of the conductor determines R:

$$R = \frac{2R_s}{\pi d} \frac{s/d}{\sqrt{(s/d)^2 - 1}} \quad [7]$$

where R_s is the surface resistance at the larmor frequency (22). For copper, $R_s = 2.61 \times 10^7 \sqrt{f}$. For the 26AWG dual conductor wire ($d = 0.5$ mm, $s = 1.6$ mm), the value R is calculated as 2.8 Ω at 64 MHz. Therefore, the series impedance per unit length, Z_s, is $2.8 + j292$ Ω. Similarly, the parallel impedance per unit length, Z_p, is $0.14 - j32.9$ Ω. The characteristic impedance of the wire in the saline solution, Z_0, is $98.1 - j0.26$. The propagation constant, γ, is calculated as $0.02 + j2.98$ m^{-1}.

Noise

The real part of Z, $\Re(Z)$, represents losses in the coil and the rms voltage of the noise can be calculated as (from ref. 26):

$$V_{\text{noise}} = \sqrt{4kT\Re(Z)\Delta f} \quad [8]$$

where k is the Boltzmann constant, T is the temperature of the body, and Δf is the effective pixel bandwidth. The effect of data averaging is accounted for in effective pixel bandwidth by dividing the pixel bandwidth by the number of excitations and the number of phase encoding steps. For an imaging protocol with a matrix size of 512 × 512, a receiver bandwidth of ±16 kHz, and a number of averages (NEX) of 2, the effective pixel bandwidth is 0.06 Hz.

For the wire that we characterized, the open circuit noise voltage on the catheter coil as a function of the coil length can be calculated as shown in Fig. 4 by using Eqs. [1] and [8]. We also calculated the noise generated due to conductance of the copper by setting Z_p to infinity (dotted line). The difference between these curves will show how much noise is generated due to the currents in the blood and in the insulator. As can be seen, if the length of the catheter coil of the proposed geometry is less than 15 cm, the noise is determined by the finite conductance of the copper. For longer coils, the noise is determined by the capacitive losses. Noise increases to unacceptable levels when the coil length approaches a quarter wave-

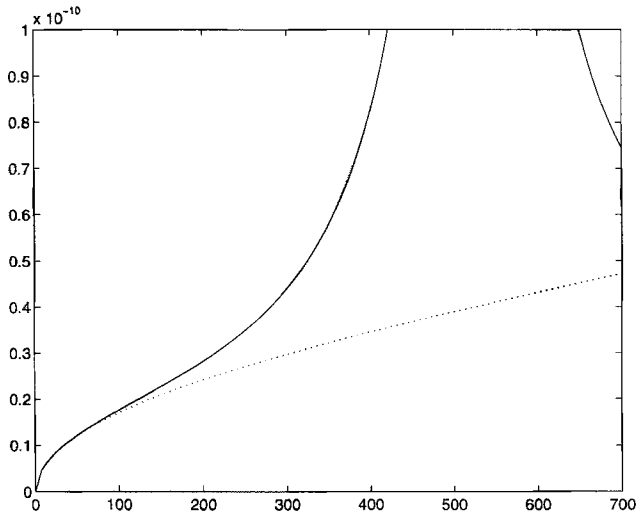

FIG. 4. Open circuit noise voltage generated on the sample catheter coil as a function of coil length (solid line). The dotted line represents the noise with no parallel impedance between the wires. Noise voltage represented by this dotted line is due to conductors. The difference between these lines shows the contribution of losses in the blood and insulator to noise. The vertical axis is the rms noise voltage, and the horizontal axis is the coil length in millimeters.

length (≈50 cm). Note that in this analysis, we assumed that the inductive losses are small. Later, we will show that this assumption is correct.

Signal. MR signal picked up with a catheter coil is a function of position of the sample and is defined as the voltage generated across the terminals of the coil due to a unit volume of water immediately after 90° RF excitation.

The signal received from a catheter coil is very high in the vicinity of conductors and drops as the distance from the conductors increases. One can use the reciprocity principle (26) to calculate the amount of signal as a function of the position in the sample. To determine the voltage generated across the terminals of the coil for a unit magnetization at point (x, y, z), the magnetic field produced at that point is calculated for an applied unit current across the coil terminal (26).

Our calculations assume that the lossy medium does not alter the magnetic and electric field distribution, the z and x-y dependence of the magnetic field is separable, and the z component is approximately proportional to the current on the conductors at that position:

$$\vec{H}(x, y, z) \approx \vec{H}_2(x, y)I(z) \qquad [9]$$

where $\vec{H}_2$ is the field perpendicular to the long axis of the conductor. For a unit RF current applied to the terminals of the coil, the current distribution along the length of the coil can be calculated by using basic transmission line theory (22):

$$I(z) = \cosh(\gamma l) - \tanh(\gamma l)\sinh(\gamma z) \qquad [10]$$

For coil lengths much smaller than the wavelength, this equation yields a current distribution that is very close to unity. Thus, the magnetic field distribution is uniform along the length of the coil. The normalized current along the length of the coil is plotted for coils of the proposed geometry, 72 mm and 1 m long in Fig. 5. The current is uniform along the length of the 72-mm coil but drops to zero around the center of the 1-m coil.

The magnetic field distribution in the x-y plane can be calculated by using basic electromagnetic theory. To simplify the equations, we assume the two conductors are infinitely long and carry unit current in opposing directions. Without loss of generality, we can assume that the conductors are along the z direction and located at positions $(s/2, 0)$ and $(-s/2, 0)$ in the x-y plane. By using Biot and Savart Law, the magnetic field at position (x, y) can be calculated for a given unit current applied to the coil terminals as:

$$\vec{H}_2(x, y) = \frac{1}{2\pi}\left(\frac{y\hat{x} - (x - s/2)\hat{y}}{y^2 + (x - s/2)^2} - \frac{y\hat{x} - (x + s/2)\hat{y}}{y^2 + (x + s/2)^2}\right) \qquad [11]$$

where $\hat{x}$ and $\hat{y}$ are the unit vectors along the x and y directions, respectively. For $s < |x^2 + y^2|$, the above equation can be simplified as:

$$\vec{H}_2(r, \theta) \approx \frac{s}{2\pi r^2}(\sin(2\theta)\hat{x} + \cos(2\theta)\hat{y}) \qquad [12]$$

where r,θ are radius and angle of the position vector. By using the reciprocity formula described in ref. 26, the open rms circuit voltage across the coil can be written as:

$$V_{oc} = -j\omega\mu M(H_x + jH_y) \qquad [13]$$

where H_x and H_y are the x and y components of the magnetic field, $\vec{H}$. μ is the magnetic susceptibility and j is

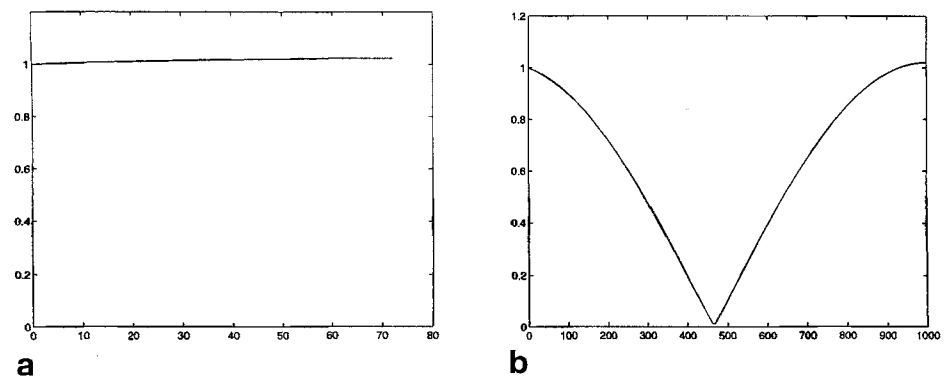

FIG. 5. Current distribution along the length of (a) 72 mm and (b) 1 m catheter coils. The current is normalized to current at the terminals of the coil. The current distribution is proportional with the sensitivity of the coil. The horizontal axis is the coil length in millimeters.

the complex number $\sqrt{-1}$. M is the total magnetization in an imaging voxel.

Signal-to-Noise Ratio

Finally, the SNR on the image can be calculated as:

$$\mathrm{SNR} = \left|\frac{V_{oc}}{V_{noise}}\right| \qquad [14]$$

Combining Eq. [14] with Eqs. [8] and [13] and assuming that the conductivity of the copper is the only noise source, one can obtain the following approximate equation:

$$\mathrm{SNR} \approx c\frac{\omega^{3/4}M}{\sqrt{\Delta f}} \cdot \frac{s}{r^2}\sqrt{\frac{d}{l}} \qquad [15]$$

where c is 5.9×10^6 m $\cdot$ s$^{1/4}$/T. In Fig. 6a, maps (the sensitivity maps) of SNR of an axial image acquired by using a catheter coil can be seen. In this calculation, we assumed a catheter coil with a length of 72 mm, a slice thickness of 3 mm, a matrix size of 512 $\times$ 512, a *TE* of 0, a *TR* of infinity, 2 excitations (NEX), a receiver bandwidth of $\pm$16 kHz, and a field of view (FOV) of 5 cm.

With similar imaging parameters (*TR*:6000 ms, *TE*: 34ms), we imaged a saline solution by using a GE Signa 1.5 T scanner with high speed gradient upgrade. We divided all the pixel values by the root mean square noise value measured on the background of the image to obtain SNR as a function of space. The contour plots of the measured SNR of the acquired images are shown in Fig. 6b. The results are in excellent agreement with our theoretical predictions shown in Fig. 6a, suggesting that the approximations and assumptions in the development of the theoretical results are valid.

If the coil is not positioned along the main magnetic field, the magnetic field $\vec{H}_2$ can be calculated by a simple coordinate transformation of Eqs. [11] or [12]. The SNR is plotted for various orientations of the coil relative to the main magnetic field, including an oblique orientation in Fig. 7. The plots show that the coil can be used to detect MR signals in all orientations relative to the main field as was shown for the opposed solenoidal coils (27).

The phase of the received signal is nonuniform. The phase map can be calculated as the argument of V_{oc} (see Fig. 8). The theoretical results agree well with the measured phase of that produced in the saline MRI experiment. The phase map also depends on the direction of the main magnetic field (see Fig. 9).

METHOD

Coil Manufacturing

We built several catheter coils from 6–8 cm and 26–30AWG dual conductor cables. For tuning and matching, small sized fixed chip capacitors (1.5 $\times$ 1.5 $\times$ 1.4 mm) were connected to the coil (see Fig. 10 for the circuit diagram). The entire coil and the capacitors were sealed with Teflon tape, heat shrink tubing, or plastic dip (see Fig. 11). A 50-ohm coaxial cable is used to transmit the MR signal to the preamplifier. For decoupling the transmit (body) and the catheter coil, a PIN diode is placed shunt to the coaxial cable at a tuned distance, l, from the matching capacitor (28). The diode can be relocated away from the coil and outside the vessel by adding a $\lambda/2$ cable. Qs of the coils were measured between 40–60 when the coils were in a saline solution. The resonance frequency decreased by about 1 MHz when the coil was loaded with the saline solution compared with what it was in air.

Uniform signal intensity image

The signal intensity of the images acquired by using the catheter coil is nonuniform. It is difficult, if not impossible, to see all the parts of the images at any one time by merely adjusting the contrast and brightness of the images. To be able to see the regions that are close to the coil, low contrast and brightness is necessary. Objects, for example, 1 cm away from the coil, cannot be seen with this adjustment and the optimum contrast and brightness level for this position causes saturation around the catheter coil.

A solution to this problem is to calculate a uniform signal intensity image by dividing the image intensity by the corresponding sensitivity map. In this case, noise on

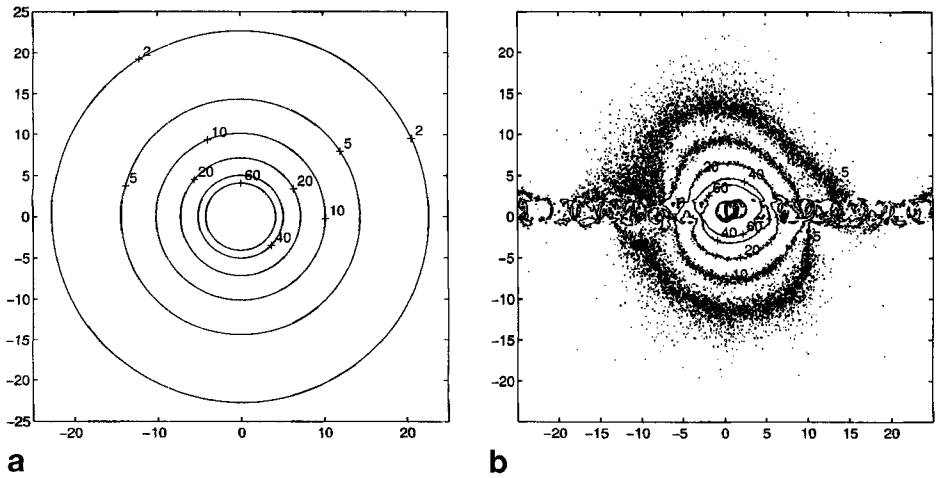

FIG. 6. The sensitivity (SNR) map of the catheter coil for slice thickness of 3 mm, matrix size of 512 $\times$ 512, TE of 0, TR of infinity, 2 NEX, receiver bandwidth of $\pm$16 kHz, and FOV of 5 cm. (a) Theoretical calculation, (b) experimental results with TR of 6000 and TE of 34 ms. All the dimensions are given in millimeters.

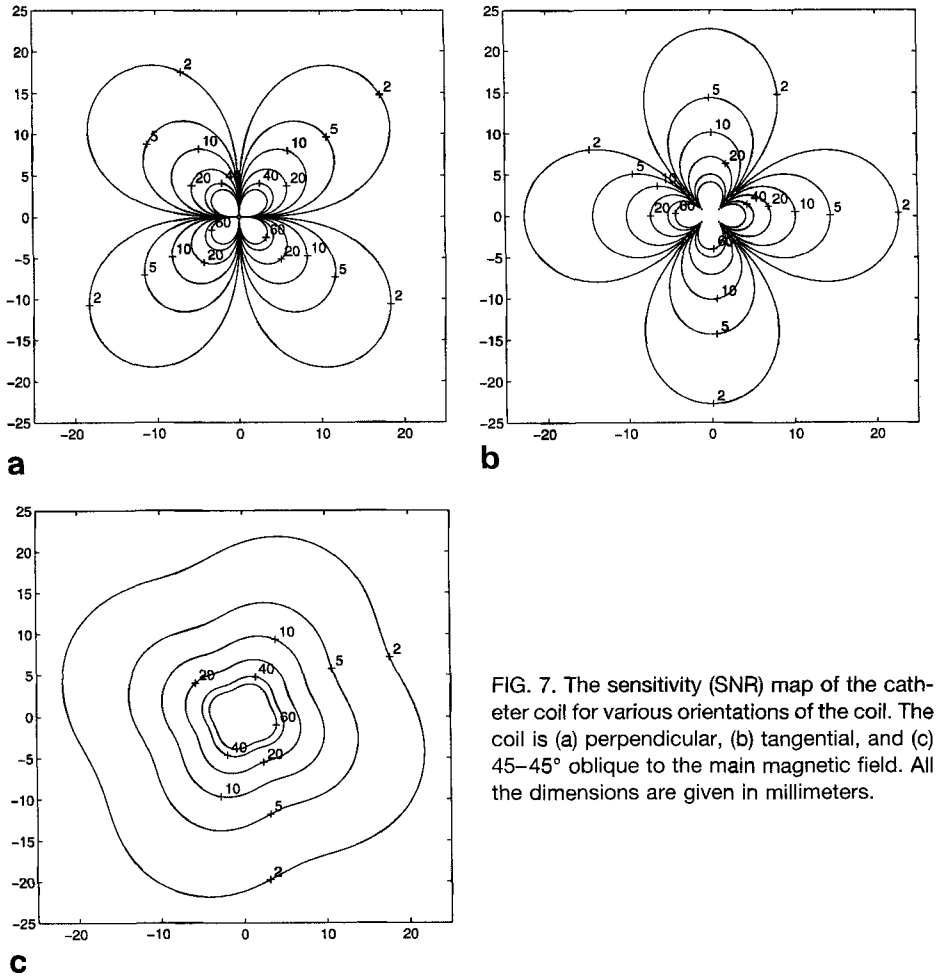

FIG. 7. The sensitivity (SNR) map of the catheter coil for various orientations of the coil. The coil is (a) perpendicular, (b) tangential, and (c) 45–45° oblique to the main magnetic field. All the dimensions are given in millimeters.

the images is not uniform, but a single brightness and contrast level can be used for a convenient display of all the parts of the image.

This display method has been implemented as an X-windows program that reads an image, derives the main magnetic field orientation with respect to the imaging plane, and assumes that the coil is perpendicular to that plane. Coil position and angle can be entered manually with the aid of a mouse. The program computes the sensitivity map and divides the image by it.

EXPERIMENTS

High Resolution Imaging of Isolated Human Aorta

As part of a feasibility study, 16 isolated human aortas from cadavers were imaged by using the catheter coil. The aortas were kept refrigerated before the experiment for a maximum of 24 h. The aortas were secured to a plastic container by using tape, and the containers were filled with water. Corks were placed at both ends of the aortas to maintain their original shape. Small holes in the

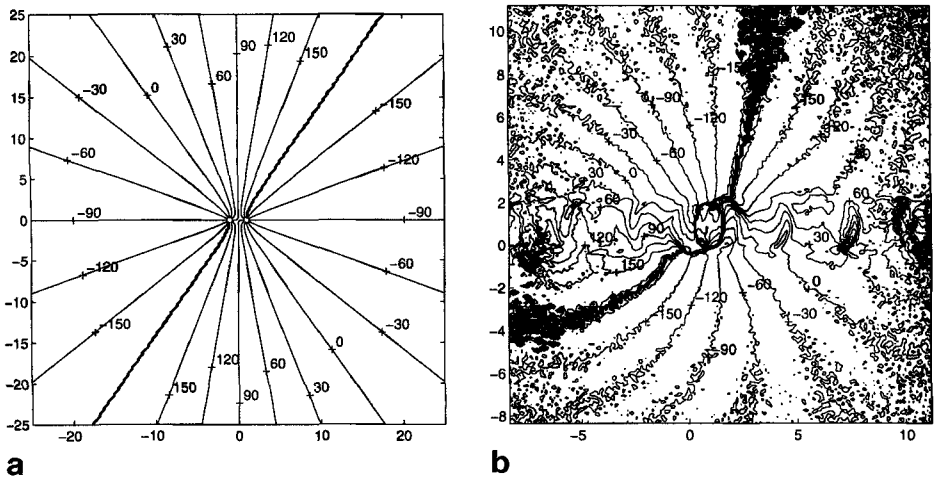

FIG. 8. The calculated and measured phase map of the catheter coil. The values represent phase in degrees of an image acquired using the catheter coil. The axes are given in mm.

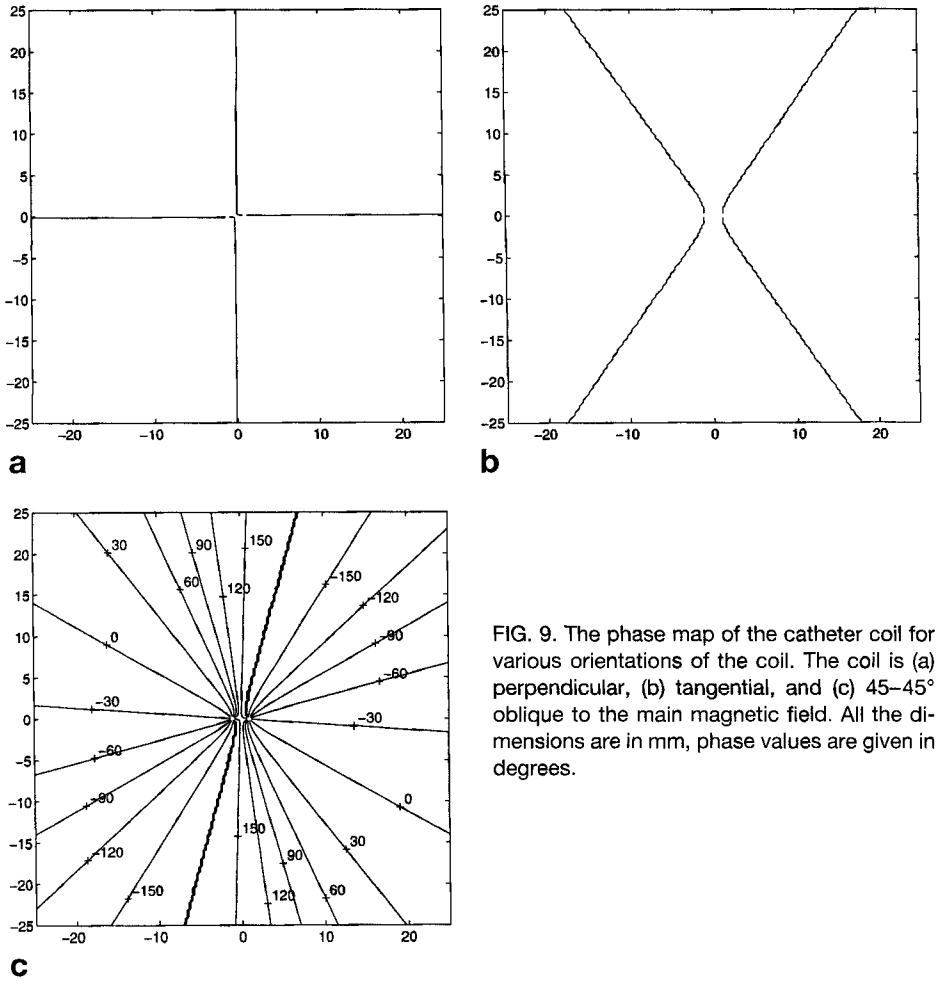

FIG. 9. The phase map of the catheter coil for various orientations of the coil. The coil is (a) perpendicular, (b) tangential, and (c) 45–45° oblique to the main magnetic field. All the dimensions are in mm, phase values are given in degrees.

corks were used to insert the catheter coil into the aorta. In the magnet, the aorta was aligned with the main magnetic field. Coronal scout images were obtained by using a fast spin-echo pulse sequence. Axial images were obtained by using the following spin-echo imaging protocol: image matrix 256 × 256; pixel dimensions 0.27 × 0.27 mm; slice thickness 3 mm; *TR* 1500 ms; two echoes; *TE* 17 and 80 ms; acquisition time 12:51; 2 NEX; and 14 slices. Uniform signal intensity images were obtained by using the signal intensity correction program described above. After the intravascular MRI, we placed a 7.5-cm surface coil just under the aorta and imaged it with the same protocol for comparison with the intravascular images.

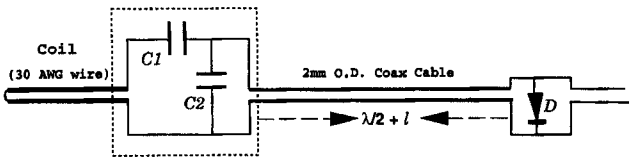

FIG. 10. The circuit diagram of the catheter coil. The tuning and matching network is composed of two capacitors. Decoupling of the coil from a transmit coil is achieved by using a diode placed shunt to the coaxial cable at a critical distance from the matching capacitor.

Two slices of the proton density and T_2-weighted human aorta images obtained by using the intravascular imaging technique are shown in Fig. 12. For comparison, the images obtained by using a 7.5-cm surface coil are shown. The profile of the catheter coil can be seen as a black region in the water. The black region just next to

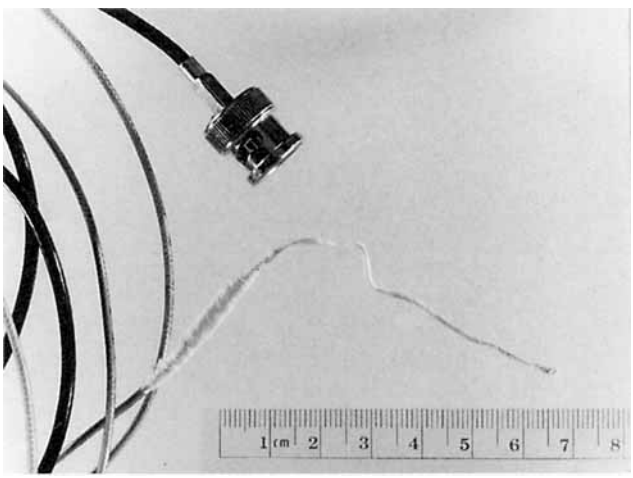

FIG. 11. A catheter coil. The coil has a diameter of 1.5 mm (4.5 French), and its tuning and matching circuit has a thickness of 3 mm (9 French).

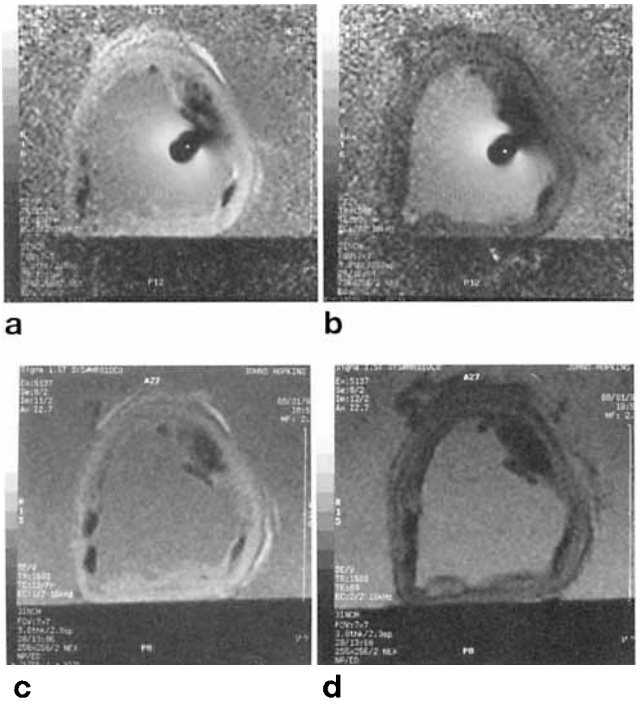

FIG. 12. Isolated human aorta images obtained using a catheter coil. (a) Proton density TR/TE 1500/17; (b) TR/TE 1500/80. The voxel size is 0.27 × 0.27 × 3 mm. Data acquisition time is 12:51. The images (c), (d) were acquired using a 7.5-cm surface coil from the same planes with the identical imaging parameters.

the coil was due to slight maladjustment of the position of the PIN diode. This was confirmed subsequently by correcting the position of the PIN diode. SNR of the images obtained by using the surface coil is more uniform than the intravascular images, therefore direct comparison of these images is not possible. In some regions, intravascular MR images gave superior SNRs. Thus, the catheter coil delivered comparable SNR to the maximum realized from a 7.5-cm surface coil and could do so at depth in the body.

The plaque that can be seen between the 1 and 3 o'clock positions was studied by histopathology (see Fig. 13). It contains intraplaque hemorrhage and calcification that cause signal void. The calcified plaque at the 4 o'clock position appears dark in both proton density and T_2-weighted images. The fibrous cap of this plaque can also be seen.

In Vivo High Resolution Imaging of a Rabbit Aorta

A 9-French (3-mm) catheter coil was inserted into the aorta of a rabbit from the lower abdomen while the animal was under general anesthesia. An image with 3-mm thickness, an FOV of 50 mm, and a matrix of 512 × 512, 2 NEX, *TR*/*TE* 1900/32 ms was obtained using a fast spin-echo pulse sequence. A magnified version of the image is shown in Fig. 14. The lumen of the aorta, as well as the root of an artery, can be seen clearly. The dark circular region around the lumen is the aortic wall. Flow artifacts are relatively small because of the saturation of blood during multi-slice imaging.

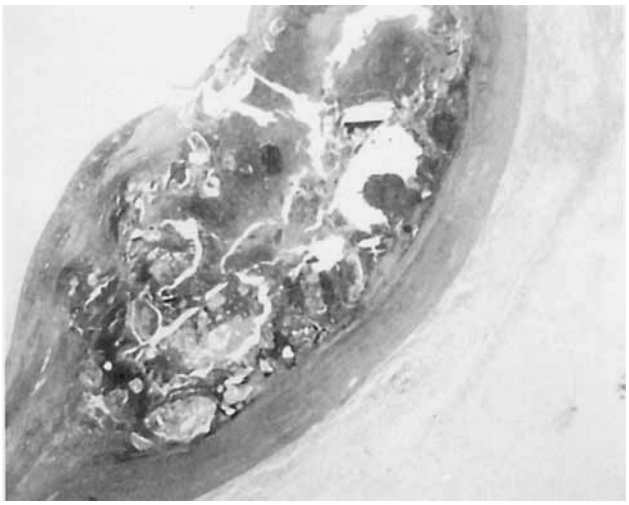

FIG. 13. Histologic section of the plaque shown in Fig. 12 between 1 and 3 o'clock position.

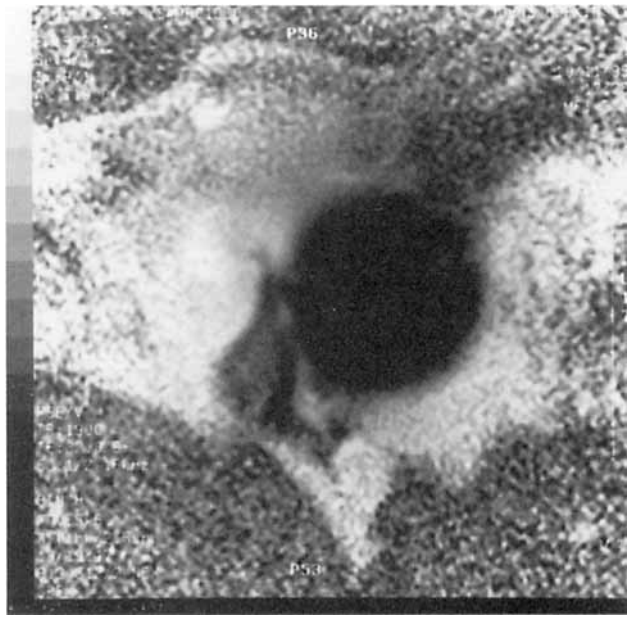

FIG. 14. *In vivo* rabbit aorta images obtained by using the catheter coil. Pulse sequence was fast spin echo with eight echo-train length. TR/TE were 1900/32 ms. Receiver bandwidth was ±16 kHz. FOV was 50 mm, and the number of excitations was 2. Matrix size was 512 × 512. The voxel size was 98 μm × 98 μm × 3 mm. Data acquisition time was 4:03.

1D CSI of Dog Coronary Artery

A set of spatially resolved chemical shift spectra was obtained by using this coil. Since the sensitivity of the coil is cylindrical, 1D chemical shift imaging (1D CSI), substantially along the length of the coil, is a logical approach. In this case, the imaging voxel is cylindrical as shown in Fig. 15. A *TR* of 2000, 140-mm FOV, and 64-phase encoding steps along the coil with 2 NEX was used. We used the body coil for transmit and the catheter coil for receive. *In situ* proton spectra from the circumflex coronary artery of an isolated normal dog heart are shown in Fig. 16. Water and lipid resonances are clearly

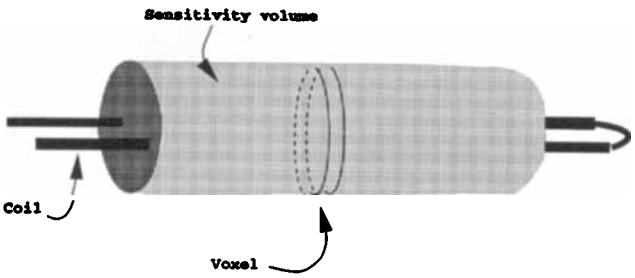

FIG. 15. The cylindrical sensitivity region of a catheter coil and a cylindrical voxel in 1D CSI.

identified. Since the phase of the coil sensitivity above the coil and under the coil oppose each other, some signal cancellation may result.

DISCUSSION

The most significant advantages of the proposed catheter coil are its small size, its high SNR, its capability to operate at any orientation with respect to the main magnetic field, its flexibility, and its extended FOV along the long axis of the coil. These features allow the coil to be used to acquire MR images and spectroscopy of small tortuous vessels such as coronary arteries. We have demonstrated very high resolution images (100 μm) with an SNR of 20 or more *in vitro* and *in vivo* in a 10-mm diameter region. We also showed localized spectra of small vessels. Our calculations show that in this catheter coil design, the dominant source of the noise is the noise generated on the copper wire. Moreover, the calculated SNR and electric properties of the coil were entirely consistent with experimental measurements.

The signal drop with distance to the coil is both an advantage and a disadvantage. Since it is not sensitive to the objects at far field, image wrap-around is not a problem in high resolution, small field-of-view images. Also, the lack of sensitivity to sources far from the coil means less noise. On the other hand, displaying the acquired images with a very bright region around the coil makes it difficult to adjust the contrast and brightness. This disadvantage has been reduced by postprocessing software that generates a uniform signal intensity image.

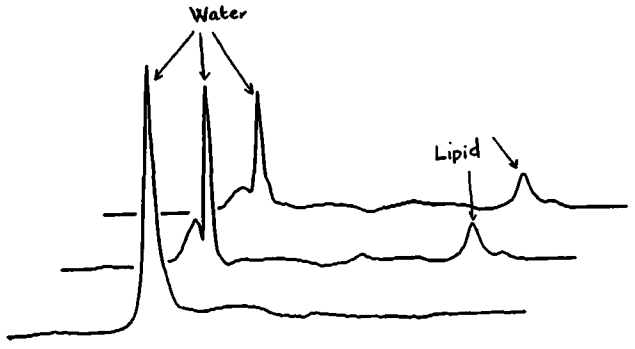

FIG. 16. The spectra of three adjacent voxels along the length of the catheter obtained by the 1D CSI technique on the isolated heart by using the catheter coil. BW was 1000 Hz, with 1024-point resolution, and the z dimension of the voxel was 2.2 mm. Radial dimension of the voxel is determined by the sensitivity of the coil. Water and lipid peaks may vary between normal and atherosclerotic vessels.

Further increases in SNR with modifications to the design are possible. Placement of an ultra-low noise preamplifier next to the coil may decrease the additive noise of the coaxial cable and preamplifier. The shorter the coil, the higher the SNR of the acquired images. This is a compromise to obtain longer coverage of the vessel of interest. A problem with very short coils is that the necessary matching and tuning capacitance values become very high.

Perhaps the most challenging problem in intravascular imaging is the issue of flow and motion artifacts. To acquire high resolution images, high strength gradient waveforms must be applied. Such pulse sequences become more sensitive to flow and motion artifacts than the standard pulse sequences. In addition, possible vibration of the coil in the vessel may increase motion artifacts. More studies must be performed to understand the effects of blood flow and physiological motion on image quality and the extent to which motion artifacts can be overcome by fast imaging methods such as EPI.

For small vessel imaging, further reduction in the size of the catheter coil is necessary. We investigated ways to produce these coils by using flexible circuit boards. The conductors of the coil as well as the matching/tuning/detuning circuit can be placed on the same flexible circuit. There is almost no practical limit on the diameter of the coil, although the reduction of the size of the tuning and matching circuit size is a challenge. An initial component search showed that the coil size can be reduced to 1.5 mm or lower. Further reduction of the size of the circuit elements may be possible with custom-designed circuit elements.

In the 1D CSI technique, the phase variation of the coil can cause signal cancellation. This problem may be eliminated by using the catheter coil for both transmission and reception. Adiabatic RF pulses will enable uniform flip angle excitation. Methods for discrimination of the pericardial from the vascular signal of the plaques will be important.

CONCLUSION

The development of new scanners has led to interventional possibilities that will require the development of intravascular devices. Interventional techniques for atherosclerotic disease may be monitored by using real-time high resolution high-speed imaging and spectroscopy techniques. In addition to precise guidance of angioplasty and atherectomy procedures, this method can be used to fully stage lesions. The goal of high resolution imaging and spectroscopy of atherosclerotic plaques can only be achieved by increasing the SNR. In this context, we designed a long and narrow flexible catheter RF coil that will have very high sensitivity to the target plaque. The design is very small in diameter and can be used in imaging and spectroscopy of small tortuous blood vessels. We theoretically calculated the SNR of the images acquired by using the catheter coil and experimentally verified our result. As a preliminary study, we used these

coils in high resolution intravascular MR imaging of isolated human aortas and a rabbit aorta *in vivo*. We also acquired chemical shift spectra from the circumflex coronary artery of a dog. Water and lipid resonances were clearly identified.

We believe that by using the intravascular MR imaging and spectroscopy system, reliable diagnostic information on atherosclerosis can be obtained and MR-guided interventions could be performed with high precision.

ACKNOWLEDGMENTS

The authors thank Robert Lin for writing the image display and signal intensity correction program and Mary McAllister for her help in manuscript preparation.

REFERENCES

1. G. S. Roubin, R. M. Califf, W. W. O'Neill, H. R. Phillips, R. S. Stack, Eds., "Interventional Cardiovascular Medicine—Principles and Practice," Churchill Livingstone, New York, 1994.
2. J. R. Spears, H. J. Marais, J. Serur, O. Pomerantzeff, R. P. Geyer, R. S. Sipzener, R. Weintraub, R. Thurer, In vivo coronary angioscopy. *J. Am. Coll. Cardiol.* **1,** 1311–1314 (1983).
3. B. F. Waller, C. A. Pinkerton, J. D. Slack, Intravascular ultrasound: a histological study of vessel during life. *Circulation* **85,** 2305–2310 (1992).
4. J. D. Pearlman, J. F. Southern, J. L. Ackerman, Nuclear magnetic resonance microscopy of atheroma in human coronary arteries. *Angiology* **42,** 726–733 (1991).
5. M. Asdente, L. Pavesi, P. L. Oreste, A. Colombo, W. Kuhn, E. Tremoli, Evaluation of atherosclerotic lesions using NMR microimaging. *Atherosclerosis* **80,** 243–253 (1990).
6. M. B. Merickel, C. S. Carman, J. R. Brookeman, J. P. Mugler, M. F. Brown, C. R. Ayers, Identification and 3-D quantification of atherosclerosis using magnetic resonance imaging. *Comput. Biol. Med.* **18,** 89–102 (1988).
7. M. B. Merickel, S. Berr, T. R. Jackson, J. Snell, P. Gillies, E. Shimshick, J. Hainer, J. R. Brookeman, C. R. Ayers, Noninvasive quantitative evaluation of atherosclerosis using MRI and image analysis. *Arterioscler. Thromb.* **13,** 1180–1186 (1993).
8. C. Yuan, J. Tsuruda, K. N. Beach, C. Hayes, M. S. Ferguson, C. E. Alpers, T. K. Foo, D. E. Strandness, Techniques for high-resolution MR imaging of atherosclerotic plaques. *J. Magn. Reson. Imaging* **4,** 43–49 (1994).
9. A. J. Martin, A. I. Gotlieb, R. M. Henkelman, High-resolution MR imaging of human arteries. *J. Magn. Reson. Imaging* **5,** 93–100 (1995).
10. M. I. Altbach, M. A. Mattingly, M. F. Brown, A. F. Gmitro, Magnetic resonance imaging of lipid deposits in human atheroma via a stimulated-echo diffusion-weighted technique. *Magn. Reson. Med.* **20,** 319–326 (1991).
11. J. G. Strang, R. J. Herfkens, G. Gold, G. Berry, J. Pauly, G. Glover, MR imaging of atherosclerotic plaques, *in* "Proc. SMR, 3rd Annual Meeting, 1995," p. 535.
12. S. Vinitski, P. M. Consigny, M. J. Shapiro, N. Janes, S. N. Smullens, M. D. Rifkin, Magnetic resonance chemical shift imaging and spectroscopy of atherosclerotic plaque. *Invest. Radiol.* **26,** 703–714 (1991).
13. C. H. Maynor, H. C. Charles, R. J. Herfkens, S. A. Suddarth, G. A. Johnson, Chemical shift imaging of atherosclerosis at 7.0 Tesla. *Invest. Radiol.* **24,** 52–60 (1989).
14. R. H. Mohiaddin, D. N. Firmin, S. R. Underwood, A. K. Abdulla, R. H. Klipstein, R. S. O. Rees, D. B. Longmore, Chemical shift magnetic resonance imaging of human atheroma. *Br. Heart J.* **62,** 81–89 (1989).
15. C. L. Dumoulin, S. P. Souza, R. D. Darrow, Real-time position monitoring of invasive devices using magnetic resonance. *Magn. Reson. Med.* **29,** 411–415 (1993).
16. V. D. Koechli, G. C. McKinnon, E. Hofmann, V. G. K, Catheters and guide wires for use in an echo-planar MR floroscopy system, *Radiology* **189(P)** 319 (1993).
17. H. L. Kantor, R. W. Briggs, R. S. Balaban, In vivo 31P nuclear magnetic resonance measurements in cacine heart using a catheter-coil. *Circ. Res.* **55,** 261–266 (1984).
18. A. J. Martin, D. B. Plewes, R. M. Henkelman, MR imaging of blood vessel with an intravascular coil. *J. Magn. Reson. Imaging* **2,** 421–429 (1992).
19. G. C. Hurst, J. Hua, J. L. Duerk, A. M. Cohen, Intravascular (catheter) NMR receiver probe: preliminary design analysis and application to canine iliofemoral imaging. *Magn. Reson. Med.* **24,** 343–357 (1992).
20. A. J. Martin, R. M. Henkelman, Intravascular MR imaging in a porcine animal model. *Magn. Reson. Med.* **32,** 224–229 (1994).
21. K. Kandarpa, P. Jakab, S. Patz, F. J. Schoen, F. A. Jolesz, Prototype miniature endoluminal mr imaging catheter. *J. Vasc. Interv. Radiol.* **4,** 419–427 (1993).
22. S. Ramo, J. R. Whinnery, T. V. Duzer, "Fields and Waves in Communication Electronics," 2nd ed., John Wiley, New York, 1984.
23. A. Chiabrera, C. Nicolini, H. P. Schwan, Eds., "Interactions between Electromagnetic Fields and Cells," vol. 97, NATO ASI Series, 1985.
24. "Catalog 93," AIN Plastics, Inc., 1993.
25. S. Kirkpatrick, J. C. D. Gelatt, M. P. Vecchi, Optimization by simulated annealing. *Science* **220,** 671–680 (1983).
26. H. Vesselle, R. E. Collin, The signal-to-noise ratio of nuclear magnetic resonance surface coils and application to a lossy dielectric cylinder model—part 1: theory. *IEEE Trans. Biomed. Eng.* **42,** 497–506 (1995).
27. J. Hua, G. C. Hurst, J. L. Duerk, T. J. Ryan, A. M. Cohen, Intravascular (catheter) NMR receiver coil: technical developments and in vivo imaging results, *in* "Proc., SMRM, 9th Annual Meeting, 1990," p. 1335.
28. W. A. Edelstein, C. J. Hardy, O. M. Mueller, Electronic decoupling of surface-coil receivers for NMR imaging and spectroscopy. *J. Magn. Reson. Imaging* **67,** 156–161 (1986).